A&A 420, 307–317 (2004)
DOI: 10.1051/0004-6361:20034267

Astronomy & Astrophysics

SOHO CDS and SUMER observations of quiescent filaments and their interpretation

G. Del Zanna[1], F. Chiuderi Drago[2], and S. Parenti[3]

[1] Department of Applied Mathematics and Theoretical Physics, University of Cambridge, UK
[2] Department of Astronomy and Space Science, University of Florence, Italy
[3] Institut d'Astrophysique Spatiale, Université de Paris Sud, 91405 Orsay Cedex, France

Received 2 September 2003 / Accepted 2 February 2004

Abstract. Three quiescent filaments located at different positions on the solar disk were selected from the SOHO CDS data archive: one of them was also observed by SUMER in the raster mode. We investigate the filament-corona transition region (PCTR) emission, to determine whether it is indeed negligible, as found in one previously-analysed case. The observations are interpreted on the basis of two different models: an isothermal (cool) prominence located above the quiet sun transition region (TR) with a portion of the corona below it, and a model composed of several cool threads embedded in the hot coronal plasma without any quiet sun TR below it. The first model indicates that, for all filaments, the PCTR emission at the top of the filament is indeed negligible, and that the chromosphere-corona TR emission under the filament is lower than the average. All filaments have similar column densities, ranging from ~2 to 7×10^{17} cm^{-2} according to model A, and from 5 to 17×10^{17} cm^{-2} according to Model B. It is not possible to determine which model better accounts for the observations, on the basis of the two prominences observed above and below the Lyman continuum limit. Model B predicts absorptions that are generally less consistent with the observations, and produces higher column densities. The comparison between the line intensities observed above and below the He I ionization limit provides an estimate of the relative neutral helium abundance N(He I)/N(H I) in the prominences.

Key words. techniques: spectroscopic – Sun: filament

1. Introduction

Observations of limb prominences and disk filaments in ultraviolet (UV), extreme ultraviolet (EUV) and microwave wavelengths provide information on the transition region between the cool gas of the prominence and the hot coronal plasma (PCTR). All UV and EUV observations performed before SOHO, except that of Schmieder et al. (1984), were of prominences at the limb (Orrall & Schmahl 1976; Engvold 1989), while most radio observations performed in the same period were of disk filaments (see references in Chiuderi Drago 1990). The results obtained in the two wavelength ranges appeared to be in conflict. In fact, the transition region line intensities measured on limb prominences were about one third of those measured on the quiet sun (QS), while the radio emission from the disk filaments appeared negligible.

To check whether this disagreement was due to a general inconsistency between UV and radio data or to a real difference between the PCTR observed off limb and on the disk, simultaneous SOHO (SUMER and CDS) and VLA (at four wavelengths between 2 and 20 cm) filament observations were performed (Chiuderi Drago et al. 2001, Paper I). The same prominence was also observed by SUMER and CDS when it was at the limb, about ten days before (Chiuderi Drago & Landi 2002).

The results of these observations can be summarized as follows: a) limb observations have shown that the transition region line intensities of the prominence are about 0.2–0.4 those of the quiet sun, in agreement with previous studies; b) disk observations have shown that the filament was clearly visible as a darker region in lines at $\lambda < 912$ Å. No intensity variation was noticed in the filament site with respect to the surrounding QS intensity at longer wavelengths. This fact was interpreted assuming that the proper emission of the PCTR at the prominence top is negligible, and that the lower intensity at $\lambda < 912$ Å was due to the Lyman continuum (L_c) absorption of the underlying quiet-Sun TR emission within the cool body of the prominence.

Filament observations seem therefore to indicate, on the same object, a difference between the PCTR emission at the side and on the top of the prominences. This has been interpreted in the framework of two different prominence models: in Chiuderi & Chiuderi Drago (1991, model A) the prominence was assumed to be isothermal, with a PCTR surrounding it,

Send offprint requests to: G. Del Zanna,
e-mail: G.Del-Zanna@damtp.cam.ac.uk

while in Chiuderi Drago et al. (1992, model B) the prominence was assumed to be formed by cool thin threads embedded in the hot coronal plasma with a tube-like TR around each of them. A similar model was already adopted by Kanno et al. (1981) to explain off-limb prominence observations. In model A, a prominence could still be thought of as composed of filamentary structures due to density fluctuations in an isothermal plasma. Note that the filamentary structure of the prominences is proved by many high-resolution images both in H_α and in UV lines (e.g. TRACE). See Chiuderi Drago et al. (1992) for references.

When a prominence is observed off-limb, it appears in emission in TR lines. At $\lambda > 912$ Å, the observed emission is the total emission of the whole PCTR. At shorter wavelengths, the average emission is lower, due to the bound-free absorption within the cool body of the prominence, as pointed out by Orrall & Schmahl (1976).

On the other hand, when a prominence is observed as a filament on the disk, the determination of the PCTR emission is not straightforward because of the many parameters affecting the observed radiation. In fact, besides the PCTR emission of the filament, $I_{\rm fil}$, the observations also depend on the following:

- the emission from the chromosphere-corona TR under the filament, $I_{\rm bg}$, which in principle can be different from the average QS emission;
- the bound-free absorption of H I and He I, at $\lambda < 912$ Å and at $\lambda < 504$ Å, respectively, which depends on the assumed prominence model.

We can eliminate the third parameter by observing the filament at $\lambda > 912$ Å, but $I_{\rm fil}$ and $I_{\rm bg}$ cannot be independently observed. We recall that, in Paper I, it was assumed $I_{\rm bg} = I_{\rm QS}$ to derive $I_{\rm fil} \sim 0$.

When spectral lines emitted at higher temperatures are considered, the modelling becomes even more complex. In fact, the reduction in the observed emission is mainly due to a combination of two effects. One is the usual bound-free absorption at $\lambda < 912$ Å, while the other one is due to the absence of coronal emission in the region where the cool prominence material is located (see Paper I and, more recently, Heinzel et al. 2003; Schmieder et al. 2003). These two effects are present also when the prominence is observed at the limb as pointed out by Kucera et al. (1998).

In this paper we analyse only the TR lines observed above three quiescent filaments, one of which is still located across the limb. The purpose of this paper is to check whether the emission from the top PCTR is indeed negligible and if it depends upon the filament position on the disk and/or on the prominence model. The PCTR emission is interpreted in the framework of the two simple models A and B mentioned above.

Note that off-limb observations of prominences show different types of structures. In some cases, prominences appear detached from the solar limb, and could well be represented by model A, while in other cases appear directly connected to the chromosphere. In principle, multi-wavelength observations of the same prominence on-disk and off-limb could provide all the information needed to characterise these structures. In practice, the temporal evolution and the projection effect at the limb make any measurements very difficult.

In the next section we describe the observations. The analysis of the bound-free continuum absorption is presented in Sect. 3, where the results obtained in Paper I are also revisited. Section 3 also contains the interpretation of the results in the framework of models A and B. A summary and the conclusions are presented in Sect. 4. Details are given in an Appendix.

Table 1. CDS and SUMER files analysed for this study.

Date	CDS files	SUMER files
Sep. 17, 1996	s4769r00	sum_960917_121122
(F1)	s4770r00	sum_960917_125727
	s4771r00	sum_960917_134359
	s4772r00	sum_960917_143030
	s4773r00	
May 9, 1998	s11068r00-01	
(F2)	s11069r00-01	
June 20, 1998	s11491r00	sum_980620_070317
(F3)	s11491r01	.....
	s11491r02	sum_980620_113223

2. Observations and data analysis

For this analysis we have searched for observations of quiescent filaments located in regions where no active regions were present. This is because we wanted to compare, on the same raster, the observed intensity above the filament with the average quiet-Sun intensity. In order to obtain a reliable measurement of the bound-free absorption, we have chosen as the primary instrument the Coronal Diagnostic Spectrometer. The CDS instrument (Harrison et al. 1995) is well-suited because it observes a large number of transition region lines in a wide range of wavelengths (150−780 Å). Here, only results from the two channels of the Normal Incidence (NIS) Spectrometer are used.

As a complementary instrument we have used SUMER (Wilhelm et al. 1995; Wilhelm et al. 1997; Lemaire et al. 1997). SUMER is a normal incidence spectrometer in the 500 to 1610 Å band thus allowing measurements above 912 Å.

We have searched the entire CDS and SUMER databases for near-simultaneous, co-spatial, on-disk observations of quiescent filaments. A large amount of data has been inspected, however, only a few datasets were found. Here results from three filaments are presented. The filaments were observed on September 17, 1996; May 9, 1998; and June 20, 1998. Let us call them F1, F2 and F3, respectively. In all the observations CDS provided monochromatic rasters of the filaments in several spectral lines. The corresponding CDS and SUMER files analysed are listed in Table 1, while Table 2 shows the CDS lines selected to measure the bound-free absorption.

The CDS and SUMER data were processed using the standard basic software within Solarsoft, and user-written routines.

Table 2. A selection of lines in the CDS/NIS wavelength bands, used in this paper. Wavelengths are taken from the CHIANTI database. When only one decimal place is indicated, the lines are blends of at least two transitions. The temperature T_e (K) of maximum ionization fraction is also indicated.

Ion	Wavelength (Å)	log T_e	NIS
Mg VII	319.027	5.8	1
Si VIII	319.825	5.9	1
Si IX	345.1	6.1	1
Fe X	345.722	6.0	1
Mg VI (bl)	349.2	5.7	1
Mg V	353.091	5.5	1
Mg VII	367.7	5.8	1
Mg IX	368.070	6.0	1
O III	525.796	5.1	2
O IV	553.329	5.3	2
O IV	554.076	5.3	2
O IV	554.513	5.3	2
O IV	555.263	5.3	2
Ca X	557.765	5.8	2
Ne VI	558.594	5.6	2
Ne VII	561.728	5.7	2
Ne VI	562.803	5.6	2
O III	599.597	5.1	2
O IV	608.397	5.4	2
Mg X	624.941	6.0	2
O V	629.732	5.4	2

In terms of calibration, note that since all measurements presented here are relative, the results are independent of the intensity calibration.

2.1. Filament F1

The Filament F1 was observed with both CDS and SUMER in rastering mode. For each instrument, a sequence of successive rasters were recorded (see Table 1).

The SUMER data are composed by sequences of O I 990.204 Å, C III 977.020 Å, L_γ 972.537 Å and N III 991.579 Å spectral windows, obtained using the $1 \times 120''$ slit and an exposure time of 25 s. The data were recorded on the *KBr* part of detector A. For this analysis, only the C III (log $T = 4.9$) and N III (log $T = 5.0$) lines were used. The SUMER rasters covered a field of view (FOV) of about $115'' \times 120''$ in a time interval of 46 min. The area of these rasters was a subset of the area covered by CDS ($122'' \times 240''$, within 36 min). The CDS and SUMER pixel sizes are approximately $2'' \times 2''$ and $1'' \times 1.1''$, respectively. The successive rasters have been analysed taking into account the solar rotation and a small offset between the pointing of the two instruments. Two sample CDS O V and SUMER C III co-spatial and near-simultaneous images are shown in Fig. 1, together with a context Hα image.

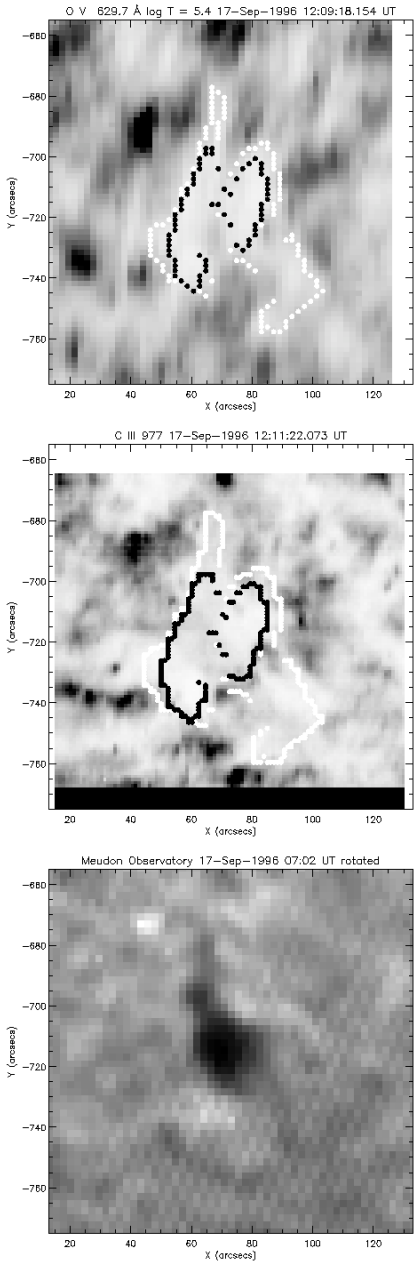

Fig. 1. From top to bottom: CDS O V and SUMER C III monochromatic (negative) images from the first rasters of the filament F1 (17 September 1996); Context Meudon H_α image. The O V image has been used to define the filament area (clearly visible as a bright region in the centre). Over-plotted on the CDS and SUMER images are the contours of two filament masks (see text), M 1 (white) and M 2 (black). For the background quiet-Sun region, we have included all image pixels except those inside the mask M 1. Note that the H_α image was taken more than five hours before the CDS and SUMER rasters, but has been rotated to simulate the position of the H_α filament during the CDS and SUMER rasters.

The filament is clearly visible in the O V rasters, while it is less defined in the SUMER images. The filament size is approximately 1−2 supergranulation cells. Quiet-Sun regions can

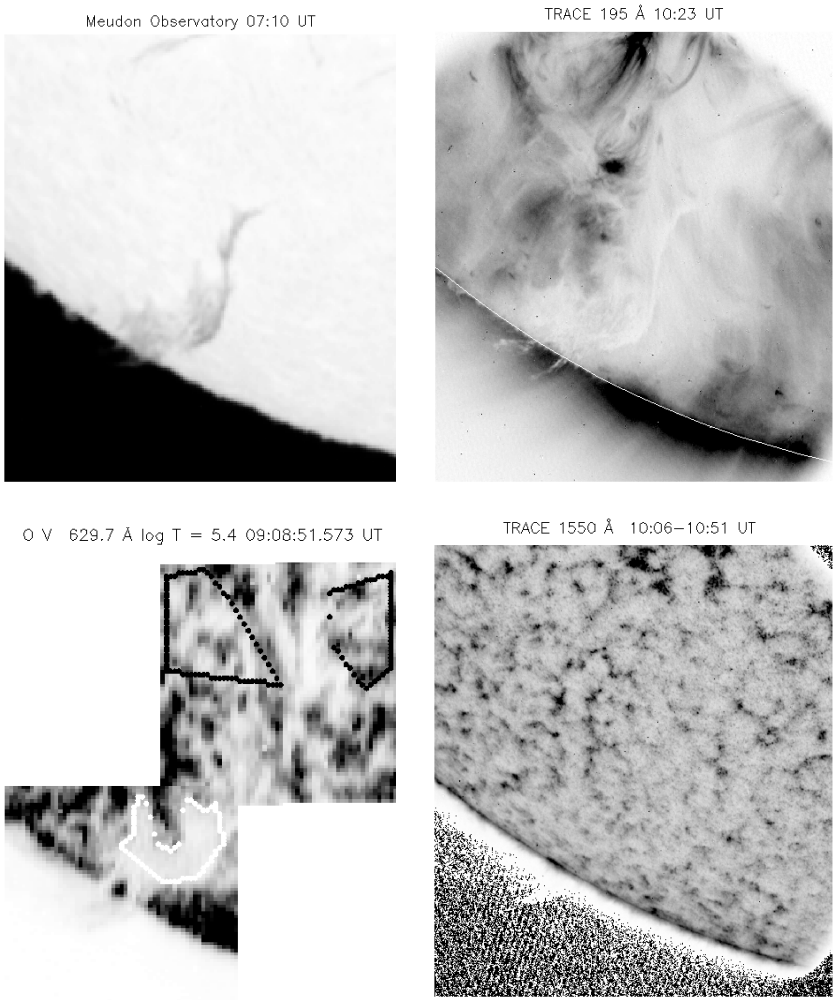

Fig. 2. H_α image, TRACE 195 Å image (negative), CDS O V monochromatic image (negative), and TRACE 1550 Å image (negative) of the filament F2 (May 9, 1998). Over-plotted on the O V image are the contours of the filament mask M 2 (white) and of the quiet Sun regions (black). Note the strong depression in the coronal lines observed in the TRACE 195 Å band, the strong absorption in the transition region line O V, and the lack of significant absorption in the C IV TRACE 1550 Å channel.

be clearly defined in the CDS rasters, but are more difficult to define in the SUMER rasters because of the smaller FOV.

The higher spatial resolution of SUMER with respect to CDS leads to a higher variability in the pixel intensity, which makes up for most of the differences between the two images (the remaining differences are due to lack of simultaneity, because of the slightly different raster durations). Given all the above, the identification of the filament and quiet-Sun areas in the SUMER rasters is more uncertain than in the CDS images.

2.2. Filaments F2 and F3

Filament F2 was observed by CDS and TRACE. It was very extended and located near the solar limb on May 9, 1998 (see Fig. 2). On this day, there are many CDS rasters, supported by TRACE observations in the three C IV filters and the L_α. A mosaic of the first 4 CDS rasters (09:08:51−12:28:40 UT, see Fig. 2) has been created for further analysis. The TRACE and CDS observations have been accurately co-aligned, by the alignment of distinct features (such as the solar limb) seen in both instruments.

Figure 3 shows H_α and CDS monochromatic images for the filament F3. This filament appears as being composed of two branches: the southern one is darker than the northern. This filament was also observed by SUMER, but not in rastering mode (i.e. with the slit position fixed). These data have been analysed, but the results are not presented here because of large uncertainties, due to the fact that the spatial extent of the slit was not sufficient to cover reference quiet Sun areas, and the co-spatiality of the SUMER and CDS data was difficult to determine.

We notice that in both Figs. 1 and 3 the filaments are narrower in H_α than in O V. In Fig. 3 the northern branch of it is almost undetected in H_α. This is due to the much larger opacity of the L_c absorption with respect to the H_α, as pointed out by Heinzel et al. (2001). As pointed out by the above authors, this fact has an important consequence: the column densities (hence the estimates of their total masses) of the filaments as derived from H_α observations are underestimated.

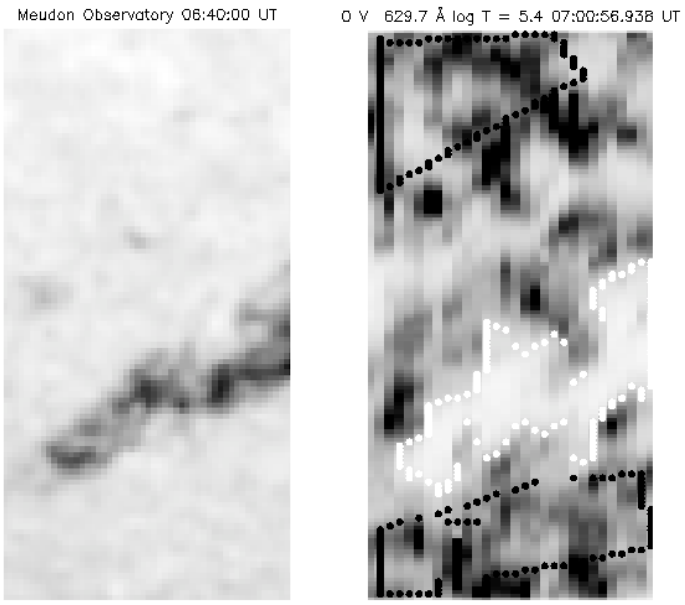

Fig. 3. H_α and CDS O V image (negative) of the filament F3 (June 20, 1998). Over-plotted on the O V image are the contours of the filament (white) and quiet sun (black) area.

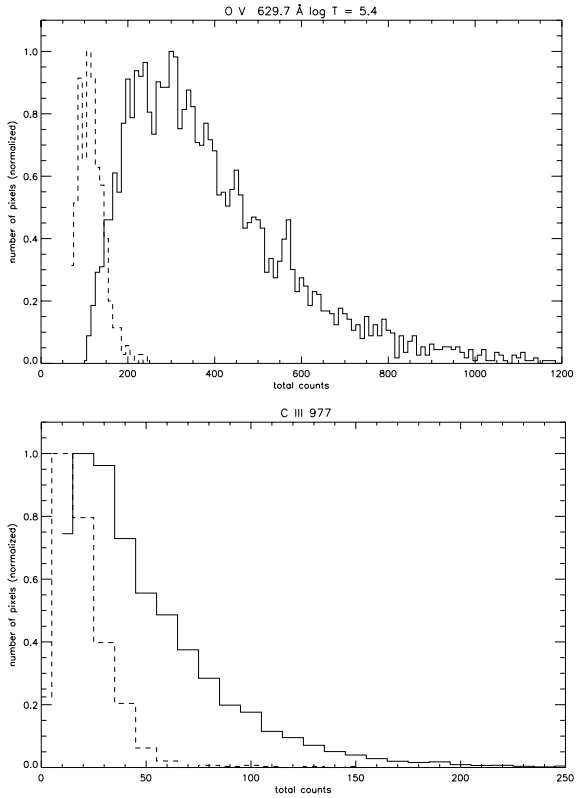

Fig. 4. Histograms of the O V and C III counts in the filament area M 2 (dashed line) and quiet Sun regions (continuous line) of the filament F1 of Fig. 1. The histograms have been normalized in order to better see the differences in the distributions of the filament and QS areas. It is evident the large absorption present in the filament area, more pronounced for O V than for C III.

2.3. Selecting the filament and QS areas

2.3.1. CDS observations

In analogy to the work carried out in Paper I, we have constructed, for all CDS rasters, monochromatic images in lines formed at $2 \times 10^4 \leq T \leq 10^6$ K. To define the filament areas, we have used for all cases the CDS O V (λ = 629 Å) images, where filaments are clearly visible. Filament areas as seen in O V are much dimmer, compared to quiet-Sun areas, as the histogram in Fig. 4 (top) shows. The O V 629 Å line was chosen because it shows the largest absorption (hence contrast) as observed by CDS. On each O V raster, we manually drew a mask following the filament contours. These masks are indicated with white contours in Figs. 1 to 3. The mask M 2 (black contour in Fig. 1) refers to a more internal and darker portion of the filament: it will be used for a comparison with the SUMER observations, as explained in the next section. Subsequently, we calculated average spectra inside each mask, and fitted them with Gaussian profiles to obtain, for each line, an average intensity $I_{\rm obs}$ over the whole filament. The same procedure has been applied to the masks identifying the quiet regions in the O V rasters, to obtain the $I_{\rm QS}$ average line intensities.

This has been repeated for all rasters belonging to F1 and F3, and for the composite image of F2. We then computed the average ratio of $I_{\rm obs}/I_{\rm QS}$ for each line in each raster.

For the reference (QS) regions, areas large enough to include cell-centre and network regions were selected. This reduces the contaminating effect of small-scale brightenings that normally occur on all time-scales in the network regions. Histograms such as those in Fig. 4 (top) have been inspected to judge the impact of mask choices on the intensity distributions. We have found that, obviously, if smaller masks including darker portions of the filament are selected, then the average $I_{\rm obs}$ decreases. This was also noticed in Paper I.

On the other hand, the QS average intensities do not sensibly change with different mask selections. Examples of selected QS masks are shown in Figs. 2 and 3. For the filament F1, we have chosen, as QS mask, the co-spatial CDS-SUMER region (excluding the portion inside mask M 1). Moreover, we have compared the absolute $I_{\rm QS}$ values in the transition region lines as obtained from all the observations and found very consistent results. In particular, the QS line intensities of the rasters of filaments F1 and F3 are very similar (differences to within a few percent), in spite of the two-year interval between the observations.

All rasters belonging to F1 and F3 provide very similar $I_{\rm obs}/I_{\rm QS}$ values even if, from one file to the other, the selected filament and QS masks are slightly different. In the following we use the values obtained by averaging the results of all files belonging to the same filament.

For the filament F2, located near the limb, the results depend very much on the choice of the mask, because of the limb-brightening effect (as discussed in the next section). For example, if a filament mask that extends up to the limb (mask M 1) is chosen, we find $I_{\rm obs} > I_{\rm QS}$ for the three shortest wavelength lines observed by NIS 1. If instead a mask that avoids the region closest to the limb is chosen (M 2, shown in Fig. 2), the ratio $I_{\rm obs}/I_{\rm QS} < 1$ at all wavelengths.

Table 3. SUMER I_{obs}/I_{QS} values for the filament F1, obtained using two different sets of filament and QS masks (see text). The values are the average over the 4 rasters.

Mask	C III	N III
MS (SUMER)	0.45 ± 0.05	0.51 ±0.07
M 2 (CDS)	0.44 ± 0.05	0.50 ±0.07

2.3.2. SUMER observations of F1

As already mentioned, for each SUMER raster, we analysed the co-spatial SUMER-CDS regions and we have assumed, in a first calculation, the filament regions coinciding with the CDS mask M 2 shown in Fig. 1 and, for the QS, the whole region outside the filament mask M 1. (The mask M 1 was not considered for the filament, due to the presence of some bight pixels inside it.) For each raster we have then calculated, as done for CDS, the average I_{obs}/I_{QS} ratios for C III and N III. The results, obtained by averaging the four rasters, are shown in the second line of Table 3.

To assess the effects of different mask selections, we have also drawn, in each C III monochromatic image, a mask identifying the darkest portion of the rasters (indicated as MS in Table 3) and a QS mask that excluded the brightest pixels. As already mentioned, due to the high spatial resolution of the SUMER instrument, we found large fluctuations, up to about 20%, of the QS average intensity from one raster to another. Using these masks we calculated the average intensities and computed the C III and N III I_{obs}/I_{QS} ratios, which are displayed in the first line of Table 3. As we can see, the results are very similar, giving us confidence that, within the uncertainties, the results are largely independent of the mask selections.

The most interesting result of these SUMER observations is the fact that, as shown in Fig. 1, the filament appears darker than the QS also at $\lambda > 912$ Å. This fact, observed both in C III and N III rasters, is also confirmed by Fig. 4 (bottom), where histograms of C III intensities in the filament and in the quiet-Sun region are shown. The histograms show that the filament and QS pixel distributions are quite distinct, although the separation is more pronounced in O V than in C III.

3. Interpretation

3.1. Model A

Let us first consider, according to model A, a loop-shaped isothermal prominence detached from the solar chromosphere and two PCTR layers, one below and one above the filament. The solar TR emission, together with the lower PCTR undergo absorption when crossing the cool gas of the prominence. The observed intensity is therefore given by:

$$I_{obs} = (I_{bg} + I_{fil})e^{-\tau} + I_{fil}. \quad (1)$$

We recall that I_{bg} and I_{fil} indicate the QS TR underneath the filament and the PCTR emission, respectively and τ is the optical thickness, mainly due to neutral hydrogen and helium ionization. Any absorption due to neutral oxygen and carbon is in fact negligible.

At $\lambda > 912$ Å practically no absorption is present and Eq. (1) becomes:

$$I_{obs}(\lambda > 912) = I_{bg} + 2 \times I_{fil}. \quad (2)$$

Observations from SUMER provide a measurement of $R = I_{obs}/I_{QS}(\lambda > 912\ \text{Å}) = I_{bg}/I_{QS} + 2I_{fil}/I_{QS}$. If we define the unknown $f = I_{fil}/I_{QS}$ we have:

$$I_{obs}/I_{QS}(\lambda < 912) = Re^{-\tau} + f(1 - e^{-\tau}) \quad (3)$$

$$I_{bg}/I_{QS}(\lambda > 912) = R - 2f \quad (4)$$

i.e. once I_{obs}/I_{QS} is measured, it is possible to derive the neutral hydrogen column density $C = \int N_{H\,I} dl$ (cm^{-2}), given that $\tau \propto C$. I_{bg} and f cannot be separately determined. In general, for $0 < I_{bg} < I_{QS}$, we have $R/2 > f > 0$.

For the filaments F1 and FP1 SUMER has provided a measurement of $R = I_{obs}/I_{QS} = 0.5$ and 1 respectively; hence f could be at maximum 0.25 and 0.5 (if $I_{bg} = 0$). For any value of $I_{bg}/I_{QS} > 0$, the upper limit of f decreases.

However, it will be shown in the following that only values of f close to its lower limit produce curves that can fit the data.

If SUMER observations are not available, we may still derive the neutral hydrogen column density C and I_{bg} using the same method used in Paper I. If we neglect, as a first approximation, the He I contribution, the optical thickness due to the Lyman continuum (L_c) absorption is given, within a 10% approximation over the entire wavelength range ($\lambda < 912$ Å), by the following relation:

$$\tau \simeq 8.36 \times 10^{-3} \lambda^3 C.$$

If we assume, as in Paper I, that $I_{fil} = 0$, a plot of $y = -\ln(I_{obs}/I_{QS})$ vs. λ^3 can be fitted by a straight line, i.e.

$$y = a + b\lambda^3$$

where $a = -\ln(I_{bg}/I_{QS})$ and the slope b is directly related to the neutral hydrogen column density C.

The y vs. λ^3 values for the three filaments presented here are plotted in Fig. 5 and the fit parameters a and b obtained using different masks are listed in Table 4. The table also includes the fitting parameters for the whole filament FP1 analyzed in Paper I. (We recall that, unlike the present case, the fit presented in Paper I was done by imposing the straight line to cross the origin, which is equivalent to assume $I_{bg} = I_{QS}$.)

We notice that all fits (except that of F2 with mask M 1) present a positive value of a indicating, in the assumption of $I_{fil} = 0$, that $I_{bg} < I_{QS}$. The negative intercept of F2 with mask M 1 is due to the strong limb brightening present under the filament ($I_{bg} > I_{QS}$). The strong dependence of I_{obs} on the underlying QS intensity makes the determination of I_{fil} on limb distance very uncertain, particularly close to the limb. Table 4 also lists the column densities C (cm^{-2}) $= 1.196 \times 10^{18} b$ (note that the horizontal axis of the plots shown in Fig. 5 is in units of Å$^3 \times 10^{-8}$).

If I_{fil} cannot be neglected with respect to I_{QS}, the observed points $y = -\ln(I_{obs}/I_{QS})$ can no longer be represented by a straight line $y = a + b\lambda^3$ as in the case when $I_{fil} = 0$.

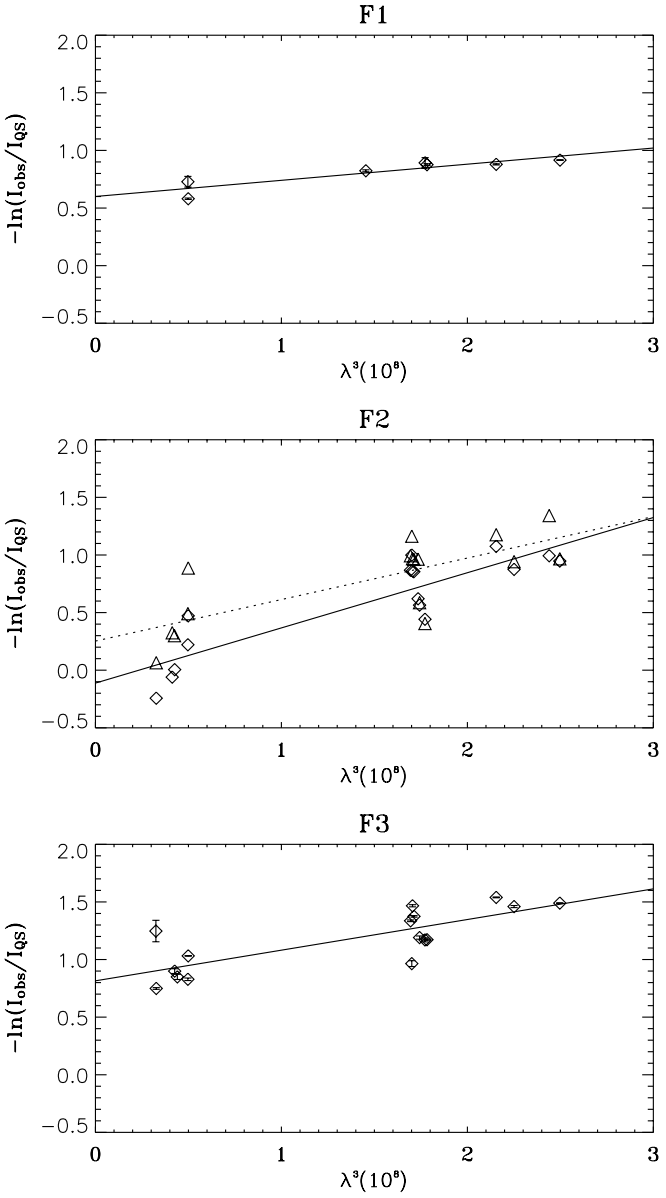

Fig. 5. Plots of $-\ln(I_{\rm obs}/I_{\rm QS})$ vs. λ^3 for the three analyzed filaments: the points in F1 and F3 plots are the average measurements over the files listed in Table 1. Notice the very little scatter in F1, where the points are obtained by averaging 5 files. In the central plot diamonds and the full line refer to the mask covering the whole filament (M 1), triangles and the dotted line to the mask excluding the filament portion lying above the limb brightening (M 2).

The data points shown in Fig. 5, mostly those referring to F1, indicate that they are consistent with a linear fit, thus confirming once more that $I_{\rm fil} \simeq 0$. The positive intercept of the fitting line a, found in all cases, except for F2 (located above the limb brightening) indicates that the QS TR emission under the filament is lower than the average. This is not surprising since at the filament site the magnetic field is horizontal and hence perpendicular to the temperature gradient, thus inhibiting the thermal conduction. It is well known that this effect reduces the TR thickness and consequently its line emission.

Another reason that could reduce the EUV line intensity observed above the filament at $\lambda > 912$ Å is the so called "volume blocking" (Schmieder et al. 2003), namely the lack of hot plasma in the volume occupied by the cool prominence. This effect is very important for coronal lines, as shown in Paper I, but probably not in the present case where we limited our analysis only to TR lines.

Table 4. Average fitting parameters for the three filaments analysed here (with the use of different masks) and the filament FP1 of Paper I.

Filament	a	b	$C(10^{17}$ cm$^{-2})$
F1 (M 1)	0.60 ± 0.05	0.14 ± 0.03	1.7 ± 0.4
F1 (M 2)	0.70 ± 0.12	0.17 ± 0.07	2.1 ± 0.8
F2 (M 1)	-0.11 ± 0.11	0.48 ± 0.07	5.7 ± 0.8
F2 (M 2)	0.25 ± 0.14	0.36 ± 0.08	4.3 ± 1.
F3	0.81 ± 0.08	0.27 ± 0.05	3.2 ± 0.6
FP1	0.37 ± 0.12	0.26 ± 0.08	3.1 ± 1.

3.2. Model B

Let us now discuss the observations assuming, according to model B, a prominence composed of N cool thin threads, each of which is surrounded by a tube-like TR. We will, moreover, assume that the prominence is bush-shaped and it rises directly up from the chromosphere without any TR emission underneath the filament ($I_{\rm bg} = 0$).

Calling I_f the TR emission and τ_f the optical thickness of each thread, and assuming that all threads are perpendicular to the line of sight, the observed intensity above the filament is given by:

$$I_{\rm obs} = I_f \left({\rm e}^{-N\tau_f} + 2{\rm e}^{-(N-1)\tau_f} + ... + 2{\rm e}^{-\tau_f} + 1 \right) = I_f H \qquad (5)$$

with

$$H = 2 \sum_{i=1}^{N-1} {\rm e}^{-(N-i)\tau_f} + {\rm e}^{-N\tau_f} + 1. \qquad (6)$$

This relation, changing τ_f into $\tau_f / \sin\theta$ also holds if the angle between the threads and the line of sight is $\theta \neq \pi/2$, provided that all the threads are roughly parallel to each other. If we assume that the optical thickness of a single thread is $\tau_f \ll 1$, while the total thickness of the prominence $\tau = N\tau_f$ may have any value, we find (see the Appendix for details):

$$I_{\rm obs} = 2NI_f \, \frac{1 - {\rm e}^{-\tau}}{\tau}. \qquad (7)$$

At $\lambda > 912$ Å no absorption is present, and we have

$$I_{\rm obs}(\lambda > 912) = 2NI_f = RI_{\rm QS} \qquad (8)$$

where, as above, the value $R = I_{\rm obs}/I_{\rm QS}$ is provided by SUMER observations at $\lambda > 912$ Å, which directly gives a measure of the total filament intensity $2NI_f$.

At $\lambda < 912$ Å, we have:

$$I_{\rm obs}/I_{\rm QS}(\lambda < 912) = R\, f(\tau) \qquad (9)$$

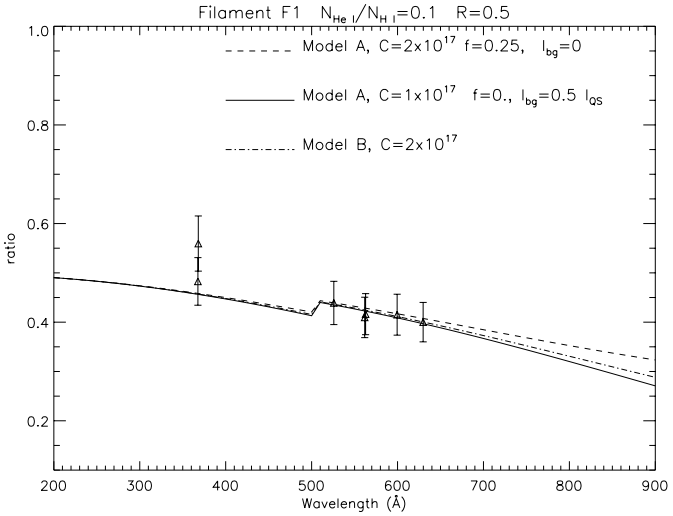

Fig. 6. Plot of the $I_{\rm obs}/I_{\rm QS}$ vs. λ data points for F1. The points are obtained by averaging 5 files. Model A (Eq. (3)) and B (Eq. (9)) are over-plotted. For model A, two limiting curves are shown. One is the curve $f = 0$, while the other one is the curve with a maximum value of f that can give a reasonable fit to the data points.

with $f(\tau) = \frac{1-e^{-\tau}}{\tau}$ from which τ and hence the neutral hydrogen column density can be directly derived from the observed ratios $I_{\rm obs}/I_{\rm QS}$, provided that SUMER observations supplying R are available. If these are not available, it is interesting to note that a plot of $-\ln f(\tau)$ vs. τ can be very well approximated, in the range $0 \le \tau \le 3$ by the straight line: $y = 0.025 + 0.419\tau$.

Therefore if the He I absorption is neglected, we may write again:

$$-\ln (I_{\rm obs}/I_{\rm QS}) = a + b\lambda^3 \tag{10}$$

with

$$a = -\ln (2NI_f/I_{\rm QS}) + 0.025$$

and

$$C = 2.85 \times 10^{18}\ b.$$

This indicates that the linear behavior of $-\ln (I_{\rm obs}/I_{\rm QS})$ vs. λ^3, shown in Fig. 5 by all filaments do not represent a constraint in favor of one of the two models. The only differences between the two models are an increase of the derived column density by a factor ~2.4 in model B with respect to model A and the different meaning of a. In model B a is directly related to the top PCTR emission: $R = 2NI_f/I_{\rm QS}$ (no background emission is in fact present).

A comparison between a and R derived from SUMER observations gives the following results: for F1, we get $R = 0.51 \pm 0.06$ from the linear fit and $R = 0.5$ from SUMER observations (see Table 3), while for FP1 we have $R = 0.71$ from the linear fit and $R \sim 1$ from SUMER observations.

A better comparison between the results obtained with the two models A and B will be discussed in the following, where we take into account the H I and He I absorption.

3.3. Including He I absorption

In the above calculations we have considered the relation between the filament intensity $I_{\rm obs}/I_{\rm QS}$, observed above and below 912 Å, with the proper filament TR emission $I_{\rm fil}$. This has been done in the framework of the two considered models and neglecting, at all wavelengths, any contribution of He I bound-free absorption to the optical thickness τ.

For lines at $228 < \lambda < 504$ Å (i.e. in the NIS 1 band), this contribution should be taken into account. Hence, for the CDS wavelengths,

$$\tau = \sigma_{\rm H\,I} \int N_{\rm H\,I} {\rm d}l + \sigma_{\rm He\,I} \int N_{\rm He\,I} {\rm d}l \tag{11}$$

where: $\sigma_{\rm H\,I}$ and $\sigma_{\rm He\,I}$ are the photoionization cross sections for the neutral hydrogen and helium; $N_{\rm H\,I}, N_{\rm He\,I}$ are the respective number densities. Here, we have used the neutral hydrogen and helium photoionization cross sections obtained from the fits provided by Verner & Yakovlev (1995). These fits are within 1−2% of the original calculations (i.e. Karzas & Latter 1961; Fernley et al. 1987).

Observations above and below the He I ionization limit can therefore be used to obtain an indication of the relative He I/H I abundance, which in turn depends on the relative He/H abundance, and on the ionization state of the prominence plasma. We note that the ratio $N_{\rm He\,I}/N_{\rm H\,I}$ should be considered as an additional parameter. First, because the He abundance could be different from its photospheric value. Variations in the helium abundance are common, and even its photospheric value is still subject of intense debate. Second, because it is not straightforward to estimate the ionization state of the plasma. If all He and H atoms are in their neutral state, $N_{\rm He\,I}/N_{\rm H\,I} \simeq 0.1$. On the other hand, at the typical prominence temperatures, helium should be predominantly neutral, and hydrogen partly ionized. Typical values of $N_{\rm He\,I}/N_{\rm H\,I}$ are in fact in the range 0.1−0.3 (V. Andretta, priv. comm. 2003). The He I absorption was taken into account also in Paper I, but this was done assuming $N_{\rm He\,I}/N_{\rm H\,I} = N_{\rm He}/N_{\rm H} \sim 0.08$ and the correction to the inferred hydrogen column density turned out to be negligible.

In the following we compare the observed $I_{\rm obs}/I_{\rm QS}$ ratios with the expected ratios as calculated from both models. In the calculations both the H I and the He I bound-free absorption is taken into account. R is derived from SUMER observations, when available, f is varied within the ranges previously determined, while the H I column density, C, and the He I abundance N(He I)/N(H I) are left as free parameters, to be derived from the observations. The curves plotted in Figs. 6 to 9 are calculated from Eqs. (3), (9), (11).

Let us first examine the data points for F1 ($R = 0.5$), shown in Fig. 6. The data points are well explained with both models, assuming $N_{\rm He\,I}/N_{\rm H\,I} = 0.1$. Within model B, we have $2NI_f = 0.5 I_{\rm QS}$ and obtain a column density $C = 2 \times 10^{17}$ cm^{-2}, while model A gives $C = 1{-}2 \times 10^{17}$ cm^{-2}, depending on the assumed values of f. These results confirm those previously derived from the fit shown in Fig. 5. However the observations cannot discriminate between Models A and B.

For the filament FP1 ($R = 1$, see Fig. 7), the data points are sufficiently explained with $N_{\rm He\,I}/N_{\rm H\,I} = 0.15$. Within model A,

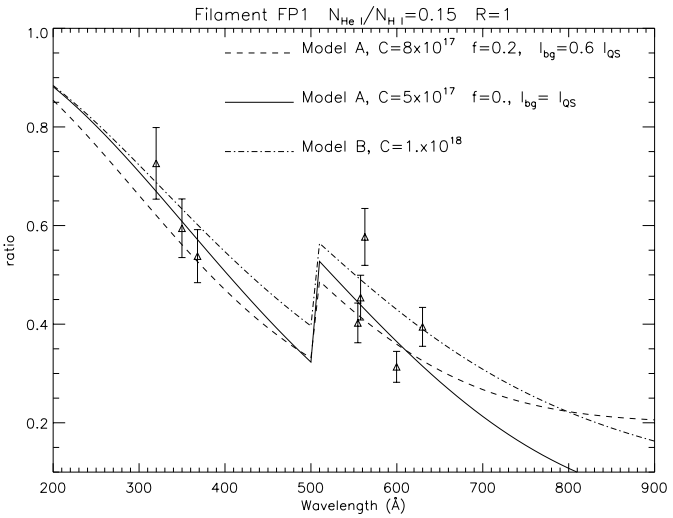

Fig. 7. Same as Fig. 6 for the filament FP1 of Paper I (mask M 1).

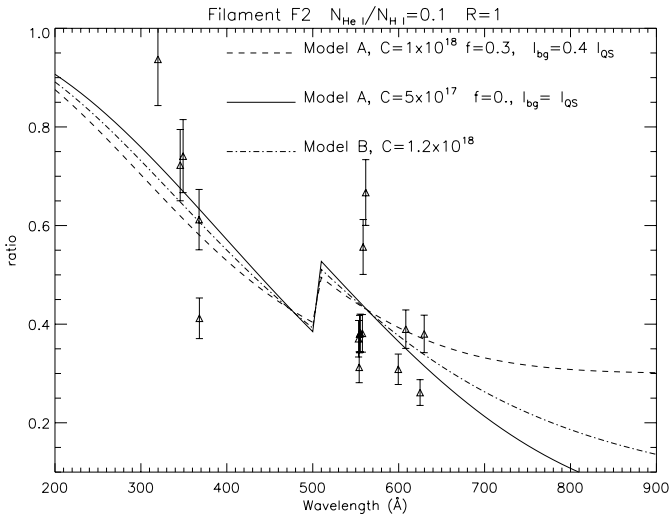

Fig. 8. Same as Fig. 6 for the filament F2.

a negligible filament emission ($f = 0{-}0.2$) fits well the data points and gives a reasonable column density $C = 5{-}8 \times 10^{17}$ cm^{-2}, similar to what found in Paper I ($f = 0$, $C = 5.5 \times 10^{17}$ cm^{-2}). Within model B, a higher $C = 1. \times 10^{18}$ cm^{-2} is required.

For F2, no SUMER data are available. However, TRACE multifilter observations could be used to estimate R. Unfortunately, the procedure to obtain C IV intensities from the multi-filter TRACE observations does not provide reliable data in the supergranular cell centres where the signal is low. However, the indication from the TRACE images is that, at $\lambda > 912$ Å, $I_{obs} \sim I_{QS}$ (i.e. $R \simeq 1$). As already mentioned, the determination of a reference I_{QS} is quite uncertain in the CDS rasters close to the limb, where it is strongly affected by the limb-brightening. A mask M 2 that avoids the portion of the filament above the strongest brightening has been selected (see Fig. 2).

Figure 8 shows the data points for F2 and the mask M 2. The model that best represents the data is model A with a negligible I_{fil}, $I_{bg} = I_{QS}$, a column density $C = 5 \times 10^{17}$ cm^{-2}, in agreement with what derived from the fit parameters of Fig. 5. However the large scatter of the data points in this case does not give us much confidence in these results. From the observations we also derive a ratio $N_{He\,I}/N_{H\,I} = 0.1$.

In case of filament F3, as mentioned, it was difficult to clearly assess R from the SUMER spectra. However the indications are for $R \simeq 1$. Assuming $R = 1$, the data points (see Fig. 9) are again best represented within model A, with $I_{fil} \sim 0$, and a column density $C = 7 \times 10^{17}$ cm^{-2} (larger by about a factor two than that derived from the fit of Fig. 5). The He I abundance in this case seems quite large: $N_{He\,I}/N_{H\,I} = 0.2$, Model B also gives a reasonable fit to the data but with a larger column density.

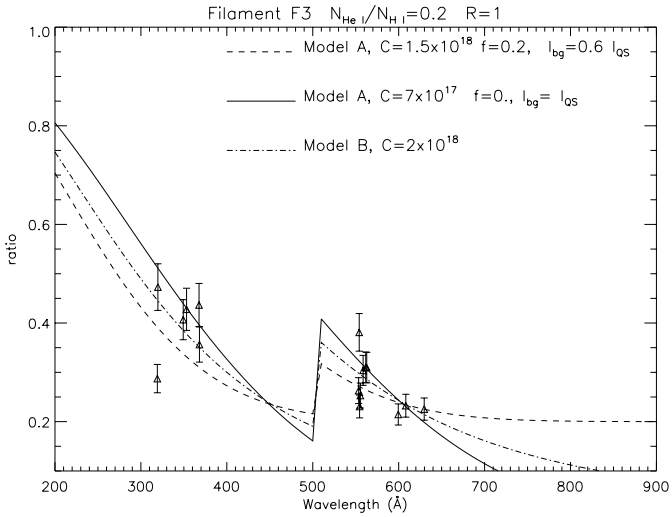

Fig. 9. Same as Fig. 6 for the filament F3.

4. Summary and conclusions

In this paper we have analysed three quiescent filaments observed by CDS and located on the disk at different distances from the limb. Two of them were also observed by SUMER, but only one in the raster mode.

The aim of this work was twofold: first to confirm the results previously found in Paper I and by Chiuderi Drago & Landi (2002), namely the negligible or absent emission from the PCTR at the filament top with respect to that measured on limb prominences (~0.3 I_{QS}). Second, to verify if the TR emission decreases slowly with increasing distance from the limb, or if it drops suddenly. Unfortunately the latter measurement was unsuccessful due to the presence of the limb brightening under the filament closest to the limb: in fact, it has been pointed out that, on disk observations, the PCTR emission and the underlying QS TR emission cannot be separately determined. It is therefore impossible to compare the PCTR emission derived from objects located at different positions on the disk with those located above the limb brightening.

We have interpreted the observations in terms of two simple prominence models. Model A consists of a loop-shaped prominence rising well above the chromosphere-corona TR, and in which the filamentary structure and the inter-thread gas

have the same temperature. The transition region surrounds therefore the whole prominence body. Model B assumes a bush-shaped prominence rising from the chromosphere (without any QS TR below it). The bush is composed of a superposition of cool threads, embedded in the hot coronal plasma, with a tube-like TR around each.

We have considered here only on-disc TR emission, and specifically avoided analysis of coronal lines, as was done instead in Paper I and, more recently, by many authors (Heinzel et al. 2003; Schmieder et al. 2003). This because the determination of the extra parameters (prominence volume and heights, cool matter filling factor etc.) was outside of the purpose of the present work.

The filaments have been analyzed, in a first approximation, taking into account only the H I absorption and using for it the approximated formula proportional to λ^3. In a second approximation using the exact expression of the H I and He I bound-free absorption coefficients. The results obtained are quite similar.

Both models can provide the neutral hydrogen column density in the prominence. Of course, to obtain the hydrogen density, an independent measurement of the filling factor would be required. Model B can give directly the total filament intensity when observed at $\lambda > 912$ Å, while in model A this quantity cannot be separated from the underlying quiet-Sun emission.

All filaments analysed here and the filament analysed in Paper I have similar characteristics. Within model A, the data points indicate that the PCTR emission at the prominence top must be negligible, and that the TR emission under the filament is lower than the average QS emission within the raster, except very close to the limb (limb brightening). All the observed filaments have similar neutral hydrogen column densities, in the range $C = 1{-}7 \times 10^{17}$ cm^{-2} according to model A. Model B predicts absorptions that are generally less consistent with the observations, and produces higher column densities.

The dimming in the TR lines observed in NIS 1 is a combination of both neutral hydrogen and helium bound-free absorption. All the observations are consistent with reasonable values of the neutral He/H ratio ($N_{\rm He\,I}/N_{\rm H\,I} = 0.1{-}0.2$). It is interesting to note that if the ionization state can be independently determined, these types of measurements can provide the He abundance.

The SUMER rasters of September 17, 1996 show that the filament appears darker than the average QS in the C III at 977 Å and N III at 991.6 Å lines. This is a new result, since previous observations (cf. Paper I) did not show any intensity variation between the filament and the surrounding QS in all lines at $\lambda > 912$ Å. The reason of this lower intensity can be ascribed to the lower emission of the TR under the filament, which could be expected since the magnetic field is horizontal.

The data points present a large scatter due to the measured intensity in the filament site and not to the average QS intensity, which has been found to be constant over a period of years. Such a large scatter prevent us in most cases to rule out one of the two models. This indicates that any model of the PCTR emission, derived from a small number of lines has a large uncertainty.

The plots shown in Figs. 6 to 9 indicate that the curves derived from the two models with different parameters, spread out at $\lambda > 650$ Å. We therefore suggest that in order to better model filament emission/absorption, future observations and instruments should cover the $\lambda > 650$ Å range, also including emission lines above the H I ionization limit. Possibly, observations should also include lines at $\lambda < 228$ Å, which would provide a constraint on the He II relative abundance. Spectroscopic observations of quiescent filaments should be done in rastering mode to allow a clear definition of the filament and QS area.

Acknowledgements. G. Del Zanna acknowledges support from PPARC. The authors wish to thank C. Chiuderi for helpful suggestions and V. Andretta for useful discussions. The authors also thank B. Schmieder for the careful reading of the manuscript and the suggestions to improve the readibility of the paper.
Part of S.P. work was made under the TOSTISP European network (contract # HPRNCT 200100310).
SOHO is a project of international collaboration between ESA and NASA. We acknowledge the use of BASS and MEDOC, the French solar databases.

5. Appendix

Let us consider the quantity

$$H = 2\sum_{i=1}^{N-1} \mathrm{e}^{-(N-i)\tau_f} + \mathrm{e}^{-N\tau_f} + 1$$

appearing in Eq. (7). Putting $k = N - i + 1$ it becomes:

$$H = 2\sum_{k=2}^{N} \mathrm{e}^{-(k-1)\tau_f} + \mathrm{e}^{-N\tau_f} + 1 = 2\sum_{k=1}^{N} (\mathrm{e}^{\tau_f})^{k-1} + \mathrm{e}^{-N\tau_f} - 1.$$

Substituting $q = \mathrm{e}^{-\tau_f}$, we know that (see for instance Gradshteyn & Ryzhik 1965):

$$2\sum_{k=1}^{N} q^{k-1} = 2\frac{q^N - 1}{q - 1}$$

and we finally get:

$$H = 2\frac{1 - \mathrm{e}^{-N\tau_f}}{1 - \mathrm{e}^{-\tau_f}} + \mathrm{e}^{-N\tau_f} - 1.$$

It can be easily checked that:

$$\lim_{\tau_f \to 0} H = 2\frac{N\tau_f}{\tau_f} = 2N.$$

Rewriting H as:

$$H = (1 - \mathrm{e}^{-N\tau_f})\frac{1 + \mathrm{e}^{-\tau_f}}{1 - \mathrm{e}^{-\tau_f}}$$

since is $\tau_f \ll 1$, we may substitute

$$\frac{1 + \mathrm{e}^{-\tau_f}}{1 - \mathrm{e}^{-\tau_f}} \simeq 2/\tau_f$$

to obtain:

$$H = 2\frac{1 - \mathrm{e}^{-N\tau_f}}{\tau_f} = 2Nf(\tau)$$

where $\tau = N\tau_f$ is the total optical depth of the filament.

References

Chiuderi, C., & Chiuderi Drago, F. 1991, Sol. Phys., 132, 81

Chiuderi Drago, F. 1990, Dynamic of Prominences, ed V. Ruzdjak, & E. Tandberg-Hanssen, Proc. IAU Coll., 117, 70

Chiuderi Drago, F., Engvold, O., & Jensen, E. 1992, Sol. Phys., 139, 47

Chiuderi Drago, F., Alissandrakis, C. E., Bastian, T., et al. 2001, Sol. Phys., 199, 115 (Paper I)

Chiuderi Drago, F., & Landi, E. 2002, Sol. Phys., 206, 315

Engvold, O. 1989, Dynamic and Structure of Quiescent Solar Prominences, ed. E. R. Priest (Kluwer Acad. pub.), 47

Fernley, J. A., Seaton, M. J., & Taylor, K. T. 1987, J. Phys. B, 20, 6457

Gradshteyn, I. S., & Rhyzik, I. M. 1965, Tables of Integral, Series and Products (Acad. Pres), 1

Harrison, R. A., Sawyer, E. C., Carter, M. K., et al. 1995, Sol. Phys., 162, 233

Heinzel, P., Schmieder, B., & Tziotziou, K. 2001, ApJ, 561, L223

Heinzel, P., Anzer, U., & Schmieder, B. 2003, Sol. Phys., 216, 159

Kanno, M., Withbroe, G. L., & Noyes, R. W. 1981, Sol. Phys., 313, 326

Karzas, W. J., & Latter, R. 1961, ApJS, 6, 167

Kucera, T. A., Andretta, V., & Poland, A. I. 1998, Sol. Phys., 183, 107

Lemaire, P., Wilhelm, K., Curdt, W., et al. 1997, Sol. Phys., 170, 105

Orrall, F. Q., & Schmahl, E. J. 1976, Sol. Phys., 50, 365

Orrall, F. Q., & Schmahl, E. J. 1979, ApJ, 231, l41

Schmieder, B., Malherbe, J. M., Mein, P., & Tandberg-Hanssen, E. 1984, A&A, 136, 1, 81

Schmieder, B., Tziotziou, K., & Heinzel, P. 2003, A&A, 401, 361

Verner, D. A., & Yakovlev, D. G. 1995, A&AS, 109, 125

Wilhelm, K., Curdt, W., Marsch, E., et al. 1995, Sol. Phys., 162, 189

Wilhelm, K., Lemaire, P., Curdt, W., et al. 1997, Sol. Phys., 170, 75